Geophysical Journal International

Geophys. J. Int. (2012) **188,** 559–569 doi: 10.1111/j.1365-246X.2011.05272.x

Instrumental evidence of normal mode rock slope vibration

Jan Burjánek,[1] Jeffrey R. Moore,[2] Freddy X. Yugsi Molina[2,3] and Donat Fäh[1]

[1] *Swiss Seismological Service, ETH Zürich, Sonneggstrasse* 5, CH-8092 *Zürich, Switzerland. E-mail: burjanek@sed.ethz.ch*
[2] *Geological Institute, ETH Zürich, Sonneggstrasse* 5, CH-8092 *Zürich, Switzerland*
[3] *Norwegian Geological Survey, Postboks* 6315 *Sluppen,* NO-7491 *Trondheim, Norway*

Accepted 2011 October 17. Received 2011 October 3; in original form 2011 June 30

SUMMARY

A unique field experiment was performed to constrain the seismic response of a large, potentially unstable rock slope in the southern Swiss Alps. Small-aperture seismic arrays were deployed to record ambient vibrations both inside and outside of the mapped instability boundary. The recordings were analysed by means of the high-resolution *f–k* method, site-to-reference spectral ratios and time–frequency dependent polarization analysis. All three methods indicated that the wavefield within the potentially unstable rock mass is dominated by normal mode motion (standing waves) rather than horizontal propagation of seismic waves. Both fundamental frequency and relative amplification could be recovered from ambient noise data. The observed amplification is strongly directional, and the maximum amplification is oriented perpendicular to open tension cracks mapped at the ground surface. Our results highlight site response characteristics relevant for analysis of earthquake-triggered rock slope failures.

Key words: Wavelet transform; Site effects; Wave propagation.

1 INTRODUCTION

Earthquakes are among the main triggers of landslides, and coseismic slope failures contribute significantly to earthquake-induced damage in areas of large topographic relief (Marano *et al.* 2010). Although a number of studies exist on the subject (reviewed, e.g. by Keefer 2002), most of these are focused on systematic documentation of past events. Quantitative evaluation of a slope's susceptibility to ground shaking is still typically based on simplified models, which ignore interactions between incoming waves and the topography or internal structure of the landslide mass. On the other hand, detailed numerical modelling of these phenomena requires a complex geophysical model, which can only be constrained by extensive field investigations at potential slope instabilities (e.g. Danneels *et al.* 2008; Gischig *et al.* 2011).

The objective of this study is to analyse the seismic response of a large, potentially unstable rock slope by means of ambient vibrations. The use of ambient vibration measurements has become increasingly attractive in a broad range of seismological disciplines at different scales. For example, noise tomography (i.e. noise cross-correlation) has improved the resolution of regional crustal velocity models (Bensen *et al.* 2009). Small-aperture seismic arrays are commonly employed to record ambient noise and characterize the shear wave velocity profile in shallow sediments (Tokimatsu 1997). The so-called Nakamura's method (i.e. H/V method) is often used to identify the resonant frequency of a soil column from single-station noise measurements (Nakamura 1989). Finally, eigenfrequencies of civil structures can be also extracted from records of ambient vibrations (e.g. Michel *et al.* 2010). Although the applications listed share one main advantage, relatively simple and efficient data acquisition, the underlying assumptions are very different. The key distinction is the content of ambient noise. For example, in noise tomography studies an incoherent diffusive wavefield is usually assumed (e.g. Curtis *et al.* 2006). On the contrary, coherent surface wave propagation is usually considered to dominate noise in shallow sediments (Bonnefoy-Claudet *et al.* 2006). Apparently, noise characteristics can be fundamentally different for different frequency bands. For example, Roten & Fäh (2007) showed that ambient noise measured in a deep sedimentary basin consisted of both standing waves of the entire basin and of surface waves propagating in the shallowest layers.

Several studies have also been conducted in the past decade regarding analysis of ambient vibration recordings on unstable hill slopes. Havenith *et al.* (2002) estimated resonant frequencies of a rock slope instability using single-station H/V measurements. Danneels *et al.* (2008) used small-aperture seismic arrays to measure dispersion of surface waves and subsequently invert for the shear wave velocity profile in the area of an active earth flow. Burjanek *et al.* (2010) estimated amplification factors and identified a range of resonant frequencies for a large unstable rock slope by noise polarization analysis. Renalier *et al.* (2010) applied a noise tomography method to resolve the shear wave velocity structure of a landslide composed of clayey soil deposits. Finally, Lévy *et al.* (2010) monitored the resonant frequency of an unstable rock column by analysis of the noise power spectrum, reporting measurable changes prior to column collapse. Such a variety of studies reflects the different origins of ambient vibrations in unstable slopes, and consequently the variety of related subsurface structures.

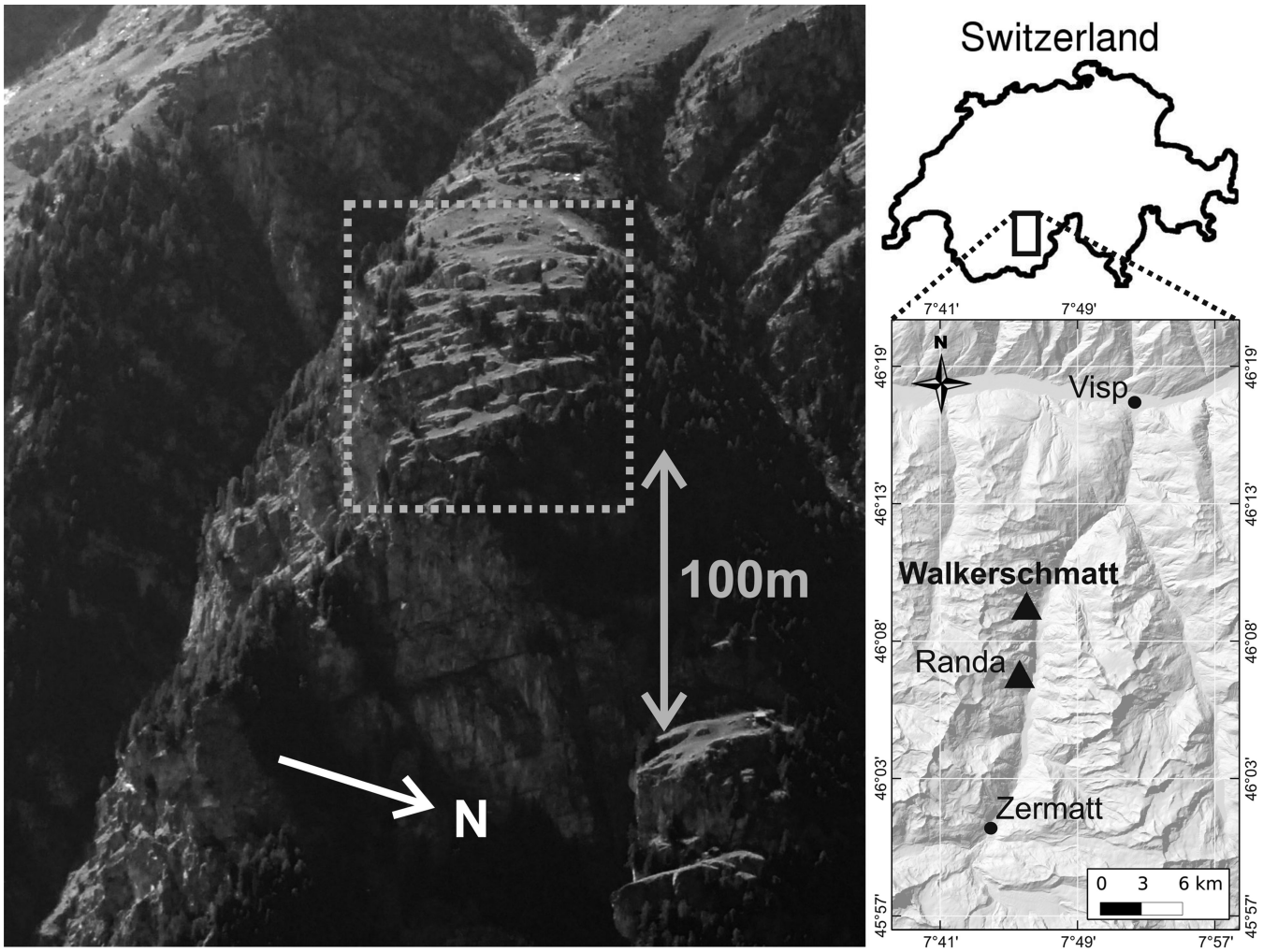

Figure 1. Photograph of the Walkerschmatt study site (view to the West from the opposite valley flank), and its location within the Matter valley (relief map at right). Seismic stations were deployed in the area surrounded by the dashed rectangle (see Fig. 2 for aerial photograph). Vertical scale is roughly represented by the double-headed arrow. The exposed eastern flank of the valley is recognizable from the relief map. The total elevation difference between mountain peaks and the adjacent valley bottom locally exceeds 3000 m.

In this paper, we follow and extend the approach introduced in our recent work at the Randa rock slope instability (Burjanek *et al.* 2010; henceforth BU10). BU10 proposed that the wavefield within an unstable rock mass may be dominated by normal mode vibration rather than horizontal propagation of seismic waves. To test this hypothesis, a new field experiment was performed at a different rock slope instability in the same region. Ambient vibration recordings were processed by means of time–frequency dependent polarization analysis (as in BU10), site-to-reference spectral ratios (SRSR) and the high-resolution *f–k* array method (Capon 1969). All three methods supported the hypothesis, and allowed us to retrieve both the fundamental frequency and relative amplification.

2 STUDY AREA

The area of canton Valais is the most seismically active region in Switzerland and home to some of the greatest topographic relief in the Alps. On average, a magnitude 6 earthquake occurs every one hundred years (Fäh *et al.* 2011). Numerous unstable rock slopes in the Matter valley area have been identified (Yugsi 2010), and a number of coseismic slope failures have been observed in previous earthquakes (Fritsche *et al.* 2006; Fritsche & Fäh 2009; Fritsche *et al.* 2010). Since the region is relatively accessible, it has been extensively studied and a solid background of relevant geological information is available (e.g. Yugsi 2010). Therefore, it is a favourable area for studying seismic triggering of landslides and site effects in unstable, hard-rock slopes.

The study site for this project, named 'Walkerschmatt', is a small topographic bench bounded by steep cliffs located near the village of St Niklaus in the Matter valley (Fig. 1). It lies 6 km north of the Randa rockslide, which was the subject of our previous study (BU10). The potential slope instability consists of an estimated 800 000–1 000 000 m^3 of crystalline rock, located within an elevation range between 1855 and 2130 m a.s.l. (Yugsi 2010). The stepped meadow at the top of the instability is transected by a network of open fractures (often with aperture >1 m) bearing record of past or ongoing deformation (see later Fig. 6). Bedrock is composed of competent orthogneiss (the so-called Randa augengneiss), a metamorphosed Permian porphyritic alkaline to subalkaline granitic intrusion constituting the core of the Penninic Siviez-Mischabel nappe (Bearth 1964), with persistent foliation (shown in black in Fig. 2) dipping gently into the slope to the S–SW (mean dip direction/dip: 240/21). The local fracture network is composed of two persistent,

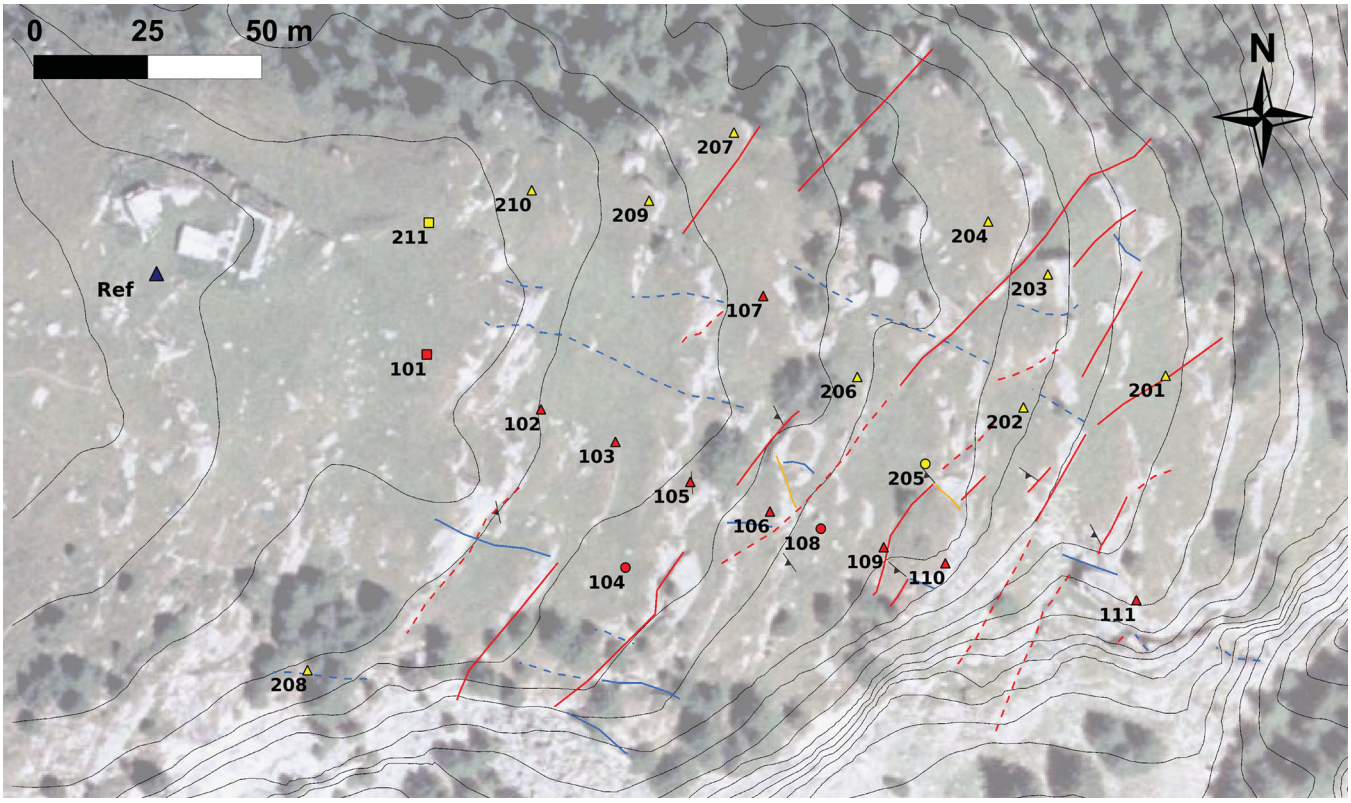

Figure 2. Configuration of the two seismic arrays (red: Array 1; yellow: Array 2; blue: Reference station). Different symbols distinguish between fully operational stations (triangles), stations without GPS time synchronization (squares), and failed stations (circles). Red, blue and orange lines represent open fractures belonging to sets J1, J2 and J3, respectively (dashed lines: inferred, solid lines: mapped). Black symbols show foliation orientation (lines parallel to strike, triangles point to dip direction). Solid black lines are contour lines with 10 m spacing.

steeply dipping joint sets J1 (132/85) and J2 (024/83) and one less persistent set J3 (067/72). Trace lengths of discontinuities in sets J1 and J2 are on the order of several tens of metres. Open fractures within the instability preferentially follow discontinuities belonging to sets J1 and J2 (red and blue lines in Fig. 2, respectively). Tension fracture aperture in the unstable rock mass increases towards the edges of the ridge, from the west (stable area) to the east and northeast. To the southeast, a few isolated unstable blocks can be found. A fault zone with orientation 036/41 is thought to act as the basal limit of the instability (not visible in Fig. 2). Precision differential GPS (GNSS) measurements conducted at the site over 10 months between 2008 and 2009 were inconclusive (displacements below the computed accuracy level), which suggests very slow rates of active deformation (Yugsi 2010).

3 FIELD EXPERIMENT

12 three-component velocity sensors with an eigenperiod of 5 s were used together with nine digital seismic systems (six channels per instrument, GPS time synchronization) to record ambient vibrations on the slope. The field experiment was carried out over 1 d in the beginning of 2009 August. The total time span of the experiment was less than 5 hr. Compass-oriented sensors were placed on metal trihedrons in shallow holes, removing superficial unconsolidated soil. The error of the sensor orientation was less than $\pm 5^{\circ}$. The precise positions of the sensors were measured with differential GPS. We progressively deployed two arrays with apertures up to 200 m (Fig. 2). The first array (WAL1) had an almost linear configuration, traversing uniformly the anticipated transition from unstable to stable areas of the slope. The geometry of the second array (WAL2) was more irregular, aimed at covering the remainder of the study site. A reference station was deployed on a small plateau within the stable portion of the slope, recording continuously throughout the day. GPS time synchronization failed at two stations WAL101 and WAL211, so precise time reference for these measurements is not available. Station WAL208 of the second array was placed on an individual rock block detached from the main part of the slope by an open fracture (aperture $\sim$1 m at the surface). Furthermore, recordings from stations WAL104, WAL108 and WAL205 were all unusable due to a sensor cable malfunction.

4 TIME–FREQUENCY POLARIZATION ANALYSIS

4.1 Method

Time–frequency polarization analysis is based on the combination of complex polarization analysis (Vidale 1986) and the continuous wavelet transform (CWT). We first use a CWT for signal time–frequency decomposition, and then apply polarization analysis on the complex wavelet amplitude for each time–frequency pair. Accurately, one should use the term 'scale' (timescale decomposition) when speaking about a CWT. However, scale can be related to Fourier frequency (e.g. Farge 1992), and here we use the terms scale and frequency interchangeably. The particle motion is then characterized for each time and frequency by an ellipse, which is generally tilted in 3-D Euclidian space. Especially the orientation of the major axis and the ellipticity are of primary interest in our

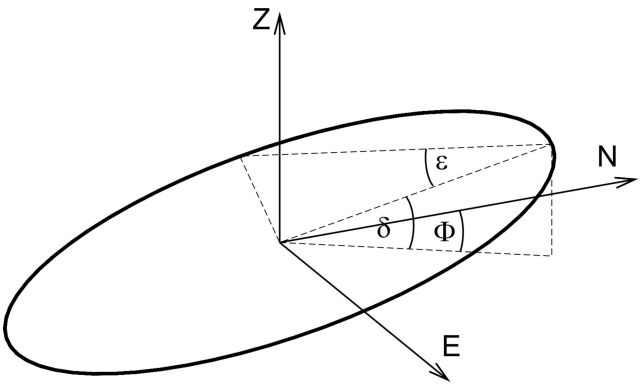

Figure 3. Particle motion is characterized for each time step and wavelet scale as an ellipse; we analyse the three parameters indicated: strike (Φ), dip (δ) and ellipticity (tan ε).

analysis. These parameters can be described by three angles (see Fig. 3): (1) azimuth of the major axis, or strike (Φ), measured in degrees from north; (2) tilt of the major axis, or dip (δ), measured in degrees downward from the horizontal and (3) ellipticity, tangent of the angle ε denoted in Fig. 3, defined as the ratio between the length of the semi-minor and semi-major axes. All three polarization parameters vary with both time and frequency. The time–frequency resolution is generally controlled by the choice of mother wavelet utilized in the CWT (e.g. Torrence & Compo 1998). The Morlet mother wavelet, a complex exponential modulated by a Gaussian envelope, was adopted in this study. The time–frequency resolution in this case is then simply controlled by changing the width of the Gaussian envelope. The presented method has the advantage of being more general than commonly used azimuthally dependent H/V spectral ratios (e.g. Del Gaudio & Wasowski 2007; Panzera *et al.* 2011).

We did not observe any systematic trends of retrieved parameters with time in our data set. Therefore we assume that observed ambient vibrations are quasi-stationary (i.e. noise properties do not change systematically on the timescale of the experiment—a few hours), and analyse the relative occurrence of polarization parameters. In particular, histograms of polarization parameters were constructed over time for each frequency (Fig. 4a). Polar plots were then adopted for the presentation of final results, which illustrate combined angular and frequency dependence (Fig. 4b). We found that histograms of ellipticity (for a single frequency band) typically resulted in an asymmetric broad peak, which was represented well by a beta distribution. Parameters of the beta distribution could be estimated for each frequency by standard statistical methods (e.g. the maximum likelihood method). In this study, we applied the method-of-moments, where the parameter estimate is based on the sample mean and variance. The estimated mode values are interconnected by a line (e.g. Fig. 5c) to illustrate the variation of ellipticity with frequency. The curve can be considered as a central value, whereas histograms in the background represent the scatter. Since the mode estimate is not based on histograms, it is not affected by the choice of bin size, and smoothly maps the frequency dependence.

4.2 Results

All recordings were processed in this analysis, including those from WAL101 and WAL211 that lacked time synchronization since an absolute time reference is not necessary for polarization analysis. The duration of recordings ranged from 60 to 90 min. Results for three stations (WALref, WAL209 and WAL204) are presented in Fig. 5. The locations of the three selected stations follow the anticipated transition from stable to unstable parts of the rock slope as described in Section 2. Here we discuss certain polarization features, especially with respect to the boundaries of the slope instability, and within the context of three frequency bands: 0.2–1 Hz, 1–2 Hz and 2–30 Hz. In the lowest frequency band (0.2–1 Hz), noise polarization follows a roughly northeast–southwest trend (strike $\Phi \sim 45^\circ$), remains primarily in the horizontal plane (dip $\delta \sim 0^\circ$), and the ellipticity (∼0.3) does not follow any specific trend with respect to frequency. This same pattern also applies for most other stations, with some exceptions (WAL109, WAL110, WAL203 and WAL208). These stations do not have much in common, except the proximity of stations WAL109 and WAL110 (separation distance 15 m), and have greater amplitudes in this frequency range (shown in Section 5). Nevertheless, histograms are relatively fluctuating for this lowest frequency band, suggesting that even longer recording times may be required for future experiments. In the highest

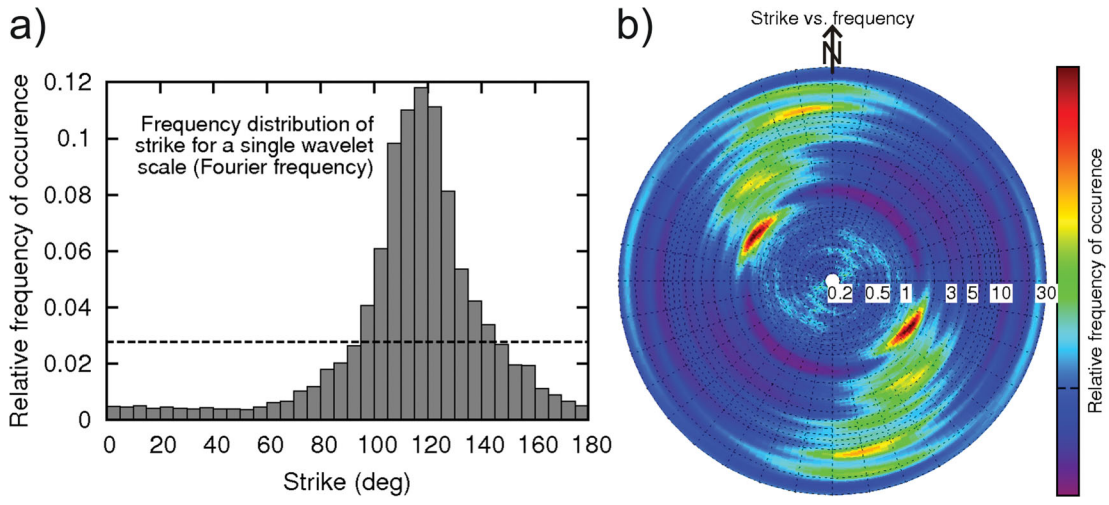

Figure 4. (a) Example histogram representing the relative occurrence of strike (azimuth) of ambient vibrations for a single wavelet scale, which is related to Fourier frequency. The dashed line represents a corresponding uniform distribution, or no preferential orientation. (b) Polar plot representation of histograms for different frequencies. The colour scale represents the relative frequency of occurrence (the height of the histogram for a given direction), and frequency changes along the radius from 0.2 to 30 Hz as indicated. The single tick within the colour scale represents the level of a uniform distribution.

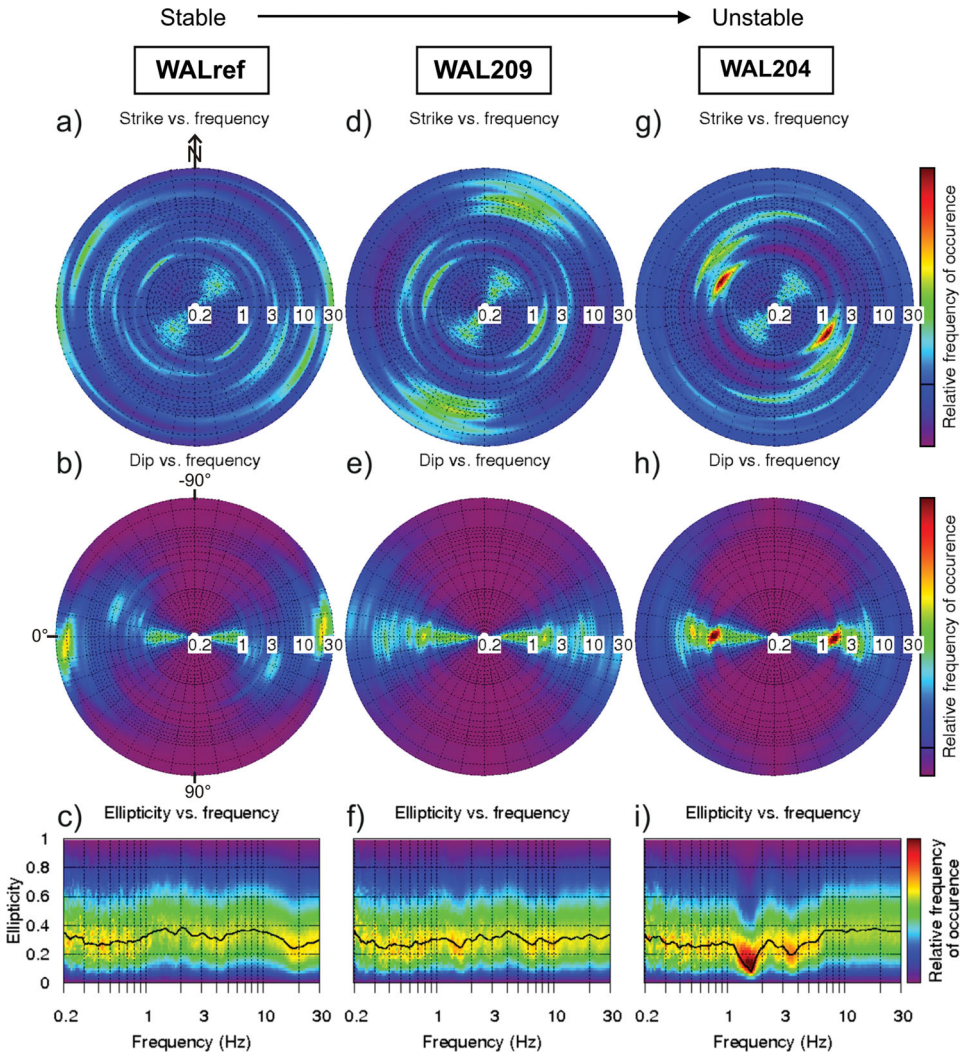

Figure 5. Results of the polarization analysis for three stations: WALref (a–c), WAL209 (d–f) and WAL204 (g–i). Colour scale represents the relative frequency of occurrence (see Fig. 4) of strike (a, d, g), dip (b, e, h) and ellipticity (c, f, i). Estimated maxima of the ellipticity distributions (assuming a beta distribution) are connected by a solid black line.

frequency range (2–30 Hz), results vary significantly from station to station, reflecting small-scale geological heterogeneity at the site. Most interesting is the intermediate frequency range (1–2 Hz). The reference station (WALref) shows only weak polarization—relatively flat and broad maxima centred around $f = 1.6$ Hz, $\Phi = 130^\circ$, $\delta = 10^\circ$ and a slight increase in ellipticity ($\sim$0.4). Moving downhill to WAL209 (see Fig. 2), the polarization peak becomes more pronounced, shifts slightly ($f = 1.6$ Hz, $\Phi = 120^\circ$ and $\delta = 5^\circ$), and a local minimum appears in ellipticity at 1.6 Hz (Fig. 5f). Finally, moving farther into the suspected unstable area at station WAL204, ellipticity drops to almost zero at 1.6 Hz and the peak becomes even more pronounced ($f = 1.6$ Hz, $\Phi = 120^\circ$ and $\delta = 5^\circ$).

Histograms of polarization strike (Φ) in the intermediate frequency range (1–2 Hz) are shown for all stations in Fig. 6, together with mapped tension cracks traversing the site. The histogram peak around 1.6 Hz oriented at $\sim$120° is present for all stations, however with different intensity. The direction 120° is approximately perpendicular to the trace of observed surface cracks. The peak intensity of strike ($f = 1.6$ Hz and $\Phi = 120^\circ$) increases systematically moving towards the east (towards the cliff). Note the relatively sharp transition in peak intensity between station pairs WAL107 and WAL207 (separation distance 35 m), and WAL102 and WAL103 (separation distance 15 m). A similarly sharp change in noise polarization across the boundary of a slope instability was also observed in our previous study (BU10), where the precise location of the border was known from years of monitoring. Thus, the difference in noise polarization response between these two station pairs may reveal the boundary between stable and unstable parts of the rock slope (shown by red arrows in Fig. 6). Moreover, noise polarization is weaker to the south (WAL103–111) as compared to the north (WAL201–206, WAL107). These two areas are separated by a persistent crack mapped at the surface (indicated by blue arrows in Fig. 6), which divides the instability into two structural compartments.

5 SITE-TO-REFERENCE SPECTRAL RATIOS

5.1 Method

Direct comparison of ground motion recordings between sites has proven to be a useful tool in a number of studies investigating

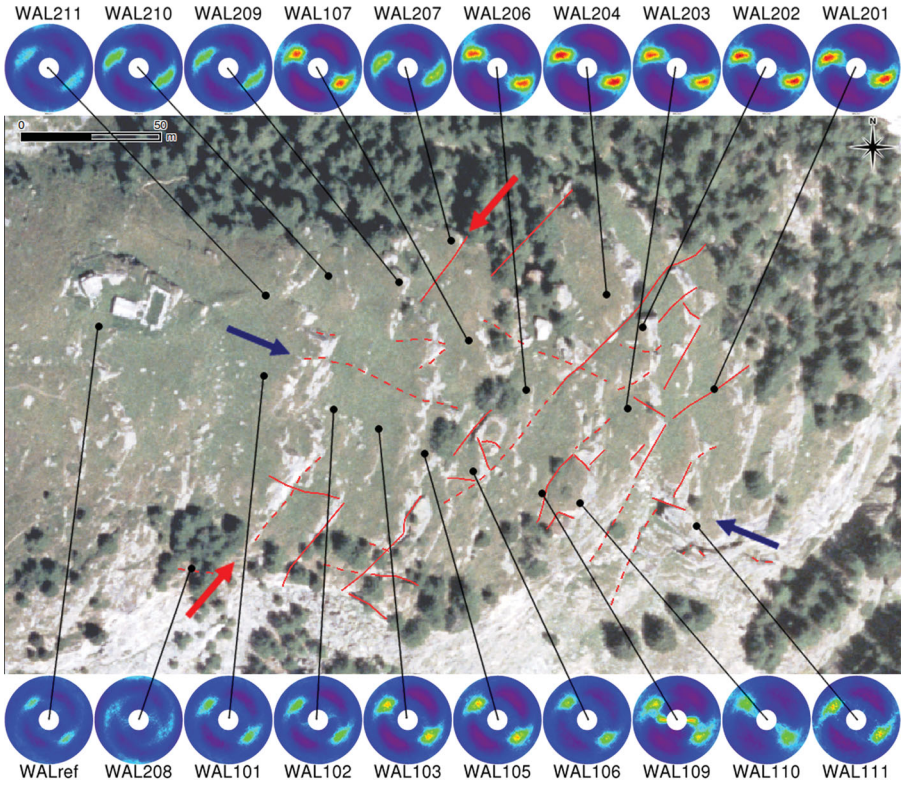

Figure 6. Distributions of ambient vibration azimuths in the frequency range of 1–2 Hz (polar plots, see Fig. 4 for explanation). Open cracks mapped at the ground surface are shown as red lines. The blue and red arrows indicate key surface cracks that delimit areas of similar polarization patterns.

local amplification due to site effects. To ensure that the observed variability in ground motion is caused by only changes in site conditions, one has to remove the variability resulting from source directivity and path effects (e.g. Andrews 1986). If the distance to the source is sufficiently large (compared to the measurement separation), radiation patterns and path effects can be neglected (Borcherdt 1970). Such comparison is often conducted from earthquake recordings, where the distance to the source is well constrained. In particular, amplitude spectra of recordings obtained at a site with known conditions (the reference site) are used to normalize spectra calculated at other sites. These so-called SRSR then represent frequency-dependent amplification functions with respect to the reference area. In analyses of ambient vibrations, precise sources are generally not known and the distant-source assumption cannot be validated. However, SRSR calculated using noise recordings can still be representative of local site conditions (e.g. Irikura & Kawanaka 1980; Roten *et al.* 2006; Roten & Fäh 2007).

Here we briefly describe the process of SRSR estimation used in this study. Time-series of ambient vibrations were split into 50 per cent overlapping windows of 100 s length and tapered with a cosine window. For each time window, the Fourier amplitude spectrum was calculated and smoothed using the window proposed by Konno & Ohmachi (1998) with a bandwidth $b = 40$. Finally the geometrical mean of ratios for all windows was determined.

5.2 Results

Horizontal components of all recordings were rotated by 120°, as this was the direction of maximum polarization identified from the previous noise polarization analysis. Recordings from stations WAL101 and WAL211 were not processed, since these were missing an absolute time reference. The resulting SRSR for three components (120°, 210° and vertical) are shown in Fig. 7. Most of the presented SRSR have reasonable, expected variation, tending towards unity at low frequencies. This is not the case, however, for station WAL110, which has more energetic horizontal components at lower frequencies (0.2–0.5 Hz). Recordings from the nearby station WAL109 also show greater amplitudes in this frequency range, suggesting that this anomaly is not caused by instrument malfunction. Station WAL110 was located precisely at the top of the cliff (Fig. 2), and it was more exposed to the wind than other stations. Moreover, a strong long-period signal on horizontal components might be related to local tilts (Forbriger 2006). Nevertheless, longer recording times would be necessary for detailed analysis, so at the moment we cannot determine the exact origin of this anomaly.

A local maximum of the SRSR (120° component) is observed at 1.6 Hz for all stations, however, the amplitude of the spectral peak is different from station to station. Interpolated maps of SRSR at 1.6 Hz are presented in Fig. 8; station WAL110 was excluded from this interpolation. A clear spatial trend is present in the 120°-component of noise. Spectral ratios increase towards the east, reaching values of 7 in the northeast corner of the site where the strongest polarization was observed (see Fig. 6). On the other hand, 210°-component spectral ratios show values <3 in the eastern part of the slope. No amplification is observed on the vertical component. Three distinct regions of the rock slope were identified in the preceding polarization analysis in the intermediate frequency range (1–2 Hz): (i) the western portion of the slope—presumably stable, with weak polarization; (ii) the northeastern area—presumably unstable, with strong polarization and (iii) the southeastern portion—also presumably unstable, with intermediate polarization. The schematic borders between these three compartments are shown

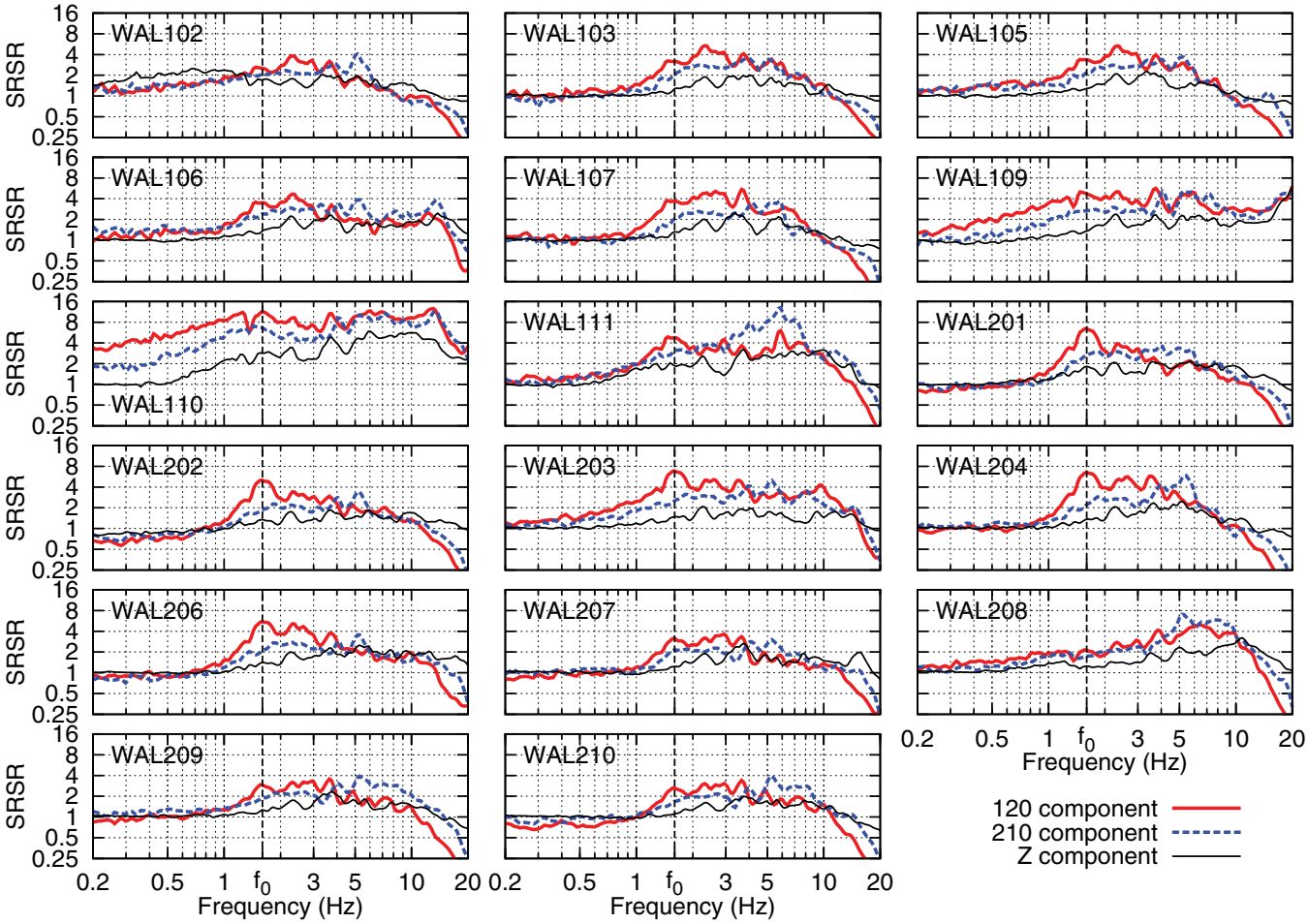

Figure 7. Site-to-reference spectral ratios for two horizontal components (120° and 210° azimuth) and the vertical component (Z) of ground motion. Dashed black line denotes the identified fundamental frequency of 1.6 Hz.

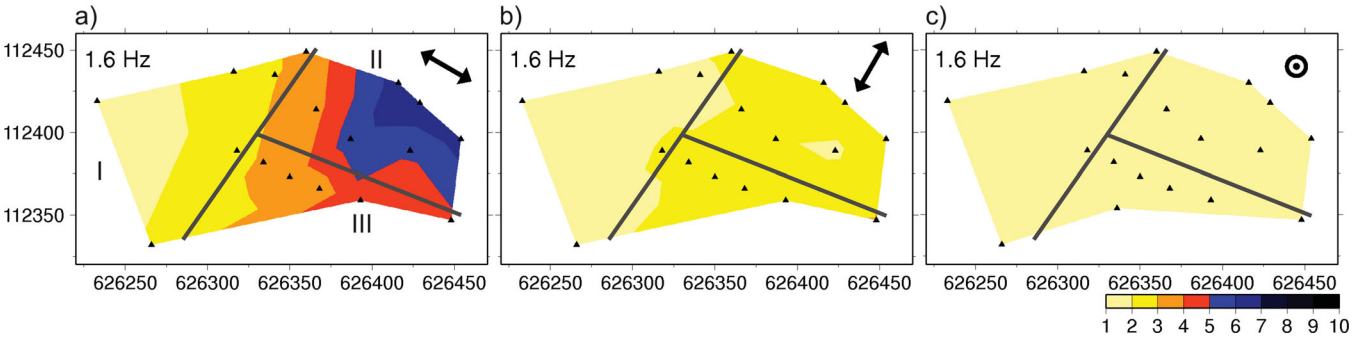

Figure 8. Interpolated map of site-to-reference spectral ratios at the fundamental frequency of 1.6 Hz for three components of ground motion [(a) 120° azimuth, (b) 210° azimuth and (c) vertical]. Grey bold lines delimit the three structural compartments (denoted by Roman numerals) identified from polarization analysis. Map coordinates are given in metres of the Swiss coordinate system.

in Fig. 8. The relative amplification factors on the 120° component can be linked to the individual compartments (I: SRSR ∼ 1–3; II: SRSR ∼ 3–7 and III: SRSR ∼ 3–5). On the other hand, there is no evident change in relative amplification between compartments II and III for the 210° component of motion (SRSR ∼ 2–3), however amplification here is still greater than in compartment I (SRSR ∼ 1–2). Spectral amplification on the vertical component shows no difference between the three compartments (SRSR < 2).

We can also identify other local maxima in the calculated spectral ratios (i.e. at 2.3, 3.7 and 5.3 Hz), which are present at almost all stations. Interpretation of these anomalies is not straightforward, since the directions of maximum amplification are not consistent across the array and the spatial pattern is complex. The decrease in spectral ratios above 15 Hz may be explained by local amplification at ∼20 Hz at the reference site (see Figs 5a–c). Finally, the resolved spectral ratios have remarkably similar shapes for several different station combinations (e.g. WAL103–105, WAL207–209-210 and WAL201–202). Such clustering may reflect additional separation of the slope into even smaller structural compartments or even individual blocks. However, objective interpretation of this complexity

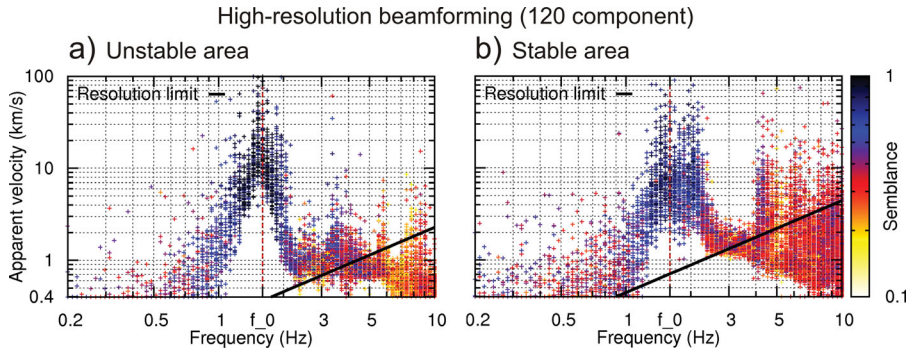

Figure 9. Apparent velocities estimated by picking maxima in the wavenumber plane for (a) subarray in the suspected unstable area of the slope (stations WAL201, 202, 203, 204, 206), (b) subarray in the suspected stable area of the slope (stations WAL207, 208, 209, 210, ref). The semblance value (level of correlation) is indicated by the colour scale. The resolution limit estimated from the array response function is shown by a black solid line. Fundamental frequency f_0 identified by polarization and SRSR analysis is shown as a dashed red line.

would require an even denser measurement grid and more detailed geological model.

6 ARRAY PROCESSING

Small-aperture seismic arrays have been widely used for characterization of the shear wave velocity structure in the shallow crust (<1 km; Tokimatsu 1997; Okada 2003; Bard *et al.* 2010). The method is particularly useful in a layered soil medium, where dispersive surface waves dominate the noise wavefield. The frequency–wavenumber (*f–k*) method is commonly used to retrieve phase velocity dispersion curves of surface waves, which are input for inversion of velocity structure. The aim of the *f–k* processing applied in this work was to identify waves propagating across the array.

6.1 Method

Generally the *f–k* method is based on a frequency–wavenumber power spectrum estimate. Assuming that the wavefield is composed of plane waves, it is possible to estimate apparent phase velocities and wave propagation directions by picking local maxima in the power spectrum (Lacoss *et al.* 1969). The power spectrum estimate is reliable only for a specific interval of wavenumbers. This interval is defined by the resolution limits of the array, which are controlled by array geometry. In principle, the lower resolution limit (minimum resolvable wavenumber) is related to the largest interstation distance (array aperture), whereas the upper resolution limit (maximum wavenumber) is related to the minimum interstation distance (station spacing). The larger and denser the array, the broader the interval of wavenumbers that can be analysed. Estimation of resolution limits has been analysed in number of previous studies (e.g. Woods & Lintz 1973; Kind *et al.* 2005; Wathelet *et al.* 2008). Moreover, the maximum likelihood estimate of power spectrum introduced by Capon (1969) can considerably improve the array resolution limits (Asten & Henstridge 1984; (Zywicki 1999), as will also be demonstrated in this paper. However, this improvement depends strongly on the characteristics of uncorrelated noise in the data set, which can usually not be anticipated. An extension to the three components of motion was proposed by Fäh *et al.* (2008) and Poggi & Fäh (2010).

In this study, we applied both classical (Lacoss *et al.* 1969) and high-resolution (Capon 1969) *f–k* power spectral estimate methods (so-called beamforming methods), as implemented by Wathelet *et al.* (2008). Recorded time-series were divided into overlapping windows of 100 s duration. A consecutive set of narrow-band filters (characterized by central frequencies f_{cent}) were applied to trace the frequency dependence. Wavenumber power spectra were then estimated for each time window and frequency band, and the location ($\boldsymbol{k}_{\mathrm{opt}}$) of the strongest peak in the spectrum was identified. Finally, an apparent velocity c_{ap} was calculated as $c_{\mathrm{ap}} = 2\pi f_{\mathrm{cent}}/|\boldsymbol{k}_{\mathrm{opt}}|$.

6.2 Results

We performed *f–k* analysis on recordings obtained by Array 2, since the geometry of Array 1 was almost linear (see Fig. 2) with a strongly asymmetric response. We focused on a subset of stations consisting of WAL201, WAL202, WAL203, WAL204 and WAL206, all located in the area of the slope near the cliff face and delimited by a distinct surface crack (Fig. 2). Horizontal components of recordings were rotated by 120° as in the previous analysis of SRSR. High-resolution *f–k* estimates of apparent velocities for the 120° component are plotted in Fig. 9(a). The level of signal correlation across the array (semblance) is indicated by the colour scale. Note the sharp increase in apparent velocity centred at ∼1.6 Hz (red dashed line), which was identified as a potential fundamental frequency of the slope instability from SRSR analysis. The apparent velocities of these highly correlated signals (semblance close to one) do not drop below 4 km s^{-1} in the narrow band between 1.4 and 1.7 Hz for any time window, and most of the points lie in the interval between 6 and 30 km s^{-1}. The lower resolution limit of the array is depicted by a solid black line, as estimated from the array response function following Wathelet *et al.* (2008). Note that all points picked below 3 Hz are beyond this resolution limit, so the observed increase in apparent velocities could be artificial. In the following, however, we argue that this is not the case.

An example of resulting wavenumber power spectra for a single time window is presented in Fig. 10. Power spectra estimated by the high-resolution *f–k* (HRBF) for three different frequency bands (centred on 1.4, 1.6 and 1.8 Hz) are depicted in Figs 10(a)–(c), respectively. Power spectra estimated by the classical *f–k* (BF) method are depicted in Figs 10(d) and (e) for two frequency bands, 1.4 and 1.6 Hz, respectively. The array response function, defined as the response of the array to a vertically propagating plane wave (e.g. Woods & Lintz 1973), is depicted in Fig. 10(f) for comparison. Resolution limits as defined by Wathelet *et al.* (2008) are indicated by the black dashed line. Open circles in the centre of the plots correspond to an apparent velocity of 4 km s^{-1}. Estimates obtained by

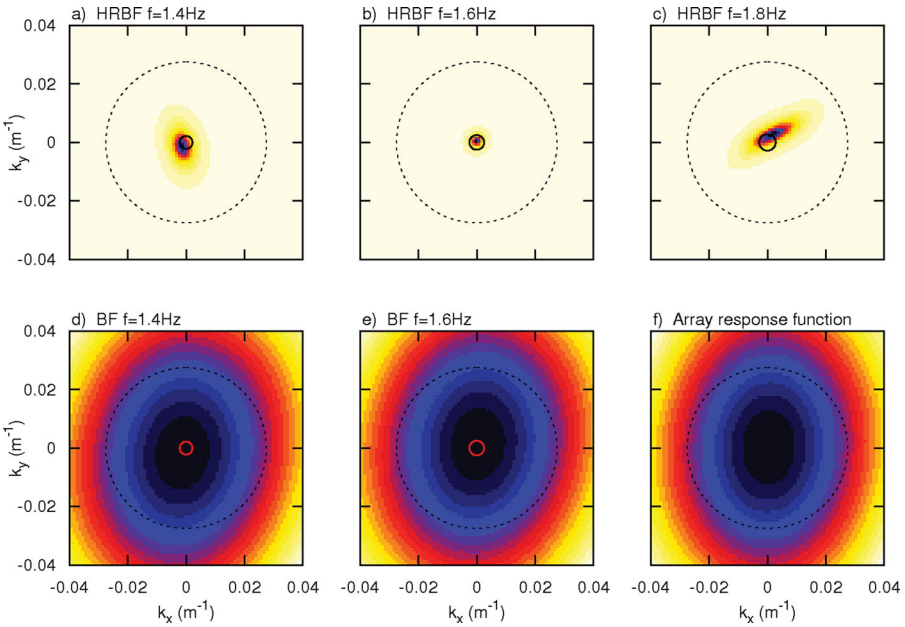

Figure 10. Normalized estimates of wavenumber power spectra for different frequencies close to the fundamental frequency (1.6 Hz) determined by both high-resolution beamforming (a, b, c) and classical beamforming (d, e) methods. The black dashed line marks the resolution limit obtained from the array response function. Black and red open circles mark the apparent velocity of 4 km s^{-1}. Power focuses towards zero wavenumber at 1.6 Hz for HRBF (b), overcoming the resolution limits shown in (f).

the classical *f–k* method are very similar for both frequencies (1.4 and 1.6 Hz), and almost undistinguishable from the array response function. On the other hand, estimates made by the high-resolution *f–k* method show clear improvement in resolution, which allows us to distinguish differences between the three frequency bands (1.4, 1.6 and 1.8 Hz). Note the considerable focusing of power towards zero wavenumber at 1.6 Hz. A similar pattern is also found for other time windows (not presented here). Thus, the increase in apparent velocities at ∼1.6 Hz presented in Fig. 9(a) is not artificial.

To summarize, observed apparent velocities of 6–30 km s^{-1} indicate that ground motion is generally in-phase at 1.6 Hz within the array. Although such high apparent velocities may indicate vertically propagating plane waves, this is not an entirely plausible interpretation in our case. The apparent velocities drop dramatically in the frequency band between 1.6 and 2 Hz (Fig. 9a), and such strong dispersion is not realistic for body waves. The *f–k* analysis was also performed using other subarray station combinations (WAL207, WAL208, WAL209, WAL210 and WALref) in the suspected stable area of the slope. Results are presented in Fig. 9(b). We also performed *f–k* analysis on other velocity components (210° and vertical). No similar sharp increase in apparent velocities was identified in either case. At frequencies above 3 Hz, no clear dispersion curve could be determined with *f–k* analysis. This indicates mechanical separation between different blocks in the unstable part of the slope, preventing the propagation of higher frequency surface waves.

7 DISCUSSION

An increasing number of studies have reported directional site effects in areas of pronounced topography (e.g. Pischiutta *et al.* 2010; Panzera *et al.* 2011), and in some cases in association with potential landslides (Del Gaudio & Wasowski 2011; Moore *et al.* 2011). However, the origin of such directionality is still not well understood in most cases. Here we take advantage of the relatively high density of observational points in our study, and explore combined interpretation of our results.

Briefly summarizing our main observations:

(1) Recorded ambient noise is polarized in a narrow frequency band centred at $f_0 = 1.6$ Hz. The preferred orientations are $\Phi_0 = 120°$ (azimuth) and $\delta_0 = 5°$ (dip), that is, polarization is mostly limited to the horizontal plane. Polarization at f_0 is strongest within the limits of the instability nearest the cliff (Fig. 6), where the particle motion is almost linear (Fig. 5i).

(2) The amplitude of the noise power spectrum increases monotonically towards the cliff at frequency f_0 and in the horizontal direction Φ_0 (Fig. 8).

(3) Ground motion is in-phase within the suspected unstable area at frequency f_0 and in the direction Φ_0 (Fig. 9).

These three attributes are typical for normal mode vibration of sedimentary basins (Bard & Bouchon 1985; Steimen *et al.* 2003, Roten *et al.* 2006), which is analogous to free oscillation of the Earth. Therefore, our observations are in agreement with the guiding hypothesis that we observe normal mode rock slope motion at the Walkerschmatt instability, as also postulated in our previous study at Randa (BU10). More specifically, we suggest that the unstable rock mass may be viewed as a volume of effectively reduced elastic moduli (fractured and damaged rock with air-filled voids). The boundary (both vertical and horizontal) between heavily fractured and more intact rock mass then presents a contrast in seismic impedance, which traps incoming waves. This results in the development of standing waves (normal mode vibration). Since the cliff presents a free surface, the greatest amplitudes of motion are found near the face (analogous to a string fixed at just one end).

However, there is a fundamental difference in comparison to sedimentary basins. Polarization of the basin normal modes has its origin in basin geometry. For example in 2-D analyses, ground motion can be separated into *SH* and *P-SV* contributions with respect to the axis of the basin (Bard & Bouchon 1985), where *SH* normal

modes are polarized parallel to the valley axis and are perpendicular to *P-SV* modes. The strong directional site response observed in this work, on the other hand, is likely caused by the fractured nature of the medium. The relationship between polarization and mapped fractures is apparent in Fig. 6. Predominant polarization of ambient noise at f_0 is in general perpendicular to observed surface cracks. We suggest that material within the unstable part of the rock slope is weakened by the cumulative effect of numerous parallel fractures, many of which can be observed at the surface. Since these cracks have a preferred orientation subperpendicular to the direction of slope displacement, effective anisotropy in rock mass moduli arises. Specifically, we suggest that the bulk stiffness of the fractured rock mass drops significantly in the direction perpendicular to the trace of tension cracks. We do not relate such an effect to inherent seismic anisotropy of the rock (e.g. due to microfracturing), but rather to the systematic orientation of open macrofractures, which are common in deep-seated rock slope instabilities. This explanation is supported by recent numerical modelling of earthquake-induced ground motion at the Randa rock slope performed by Moore *et al.* (2011). Directional amplification and polarization of ambient noise was recently observed on the flank of Mt Etna (Di Giulio *et al.* 2009; Rigano *et al.* 2008), which was also related to the presence of a fault system.

Excitation of normal mode vibration by ambient noise sources results in significant local site amplification, with spectral ratios up to 7 in the unstable area of the slope compared to the reference station on adjacent stable ground (Fig. 8). Such strong relative amplification cannot be explained by topographic site effects alone, that is, only by the shape of the topography. Previous numerical studies suggested that amplification factors rarely exceed 2 for topographic irregularities underlain by a homogeneous half-space (e.g. Geli *et al.* 1988; Assimaki *et al.* 2005). Moreover, the numerical simulation performed by Moore *et al.* (2011) required introduction of subsurface heterogeneity (compliant fractures) to explain observed amplification for an analogous case study at the Randa rock slope instability. Comparison of SRSR obtained from ambient noise and regional earthquake data (weak motion) showed good agreement in analysis of data recorded at the Randa rockslide (Moore *et al.* 2011). This is a promising outcome since acquisition of ambient vibration data is substantially more time- and cost-effective. Nevertheless, we emphasize that the slope may behave differently under strong shaking (high-strain motion). For example, high strains may result in systematic damage to the rock mass (further fracturing), which would dissipate elastic energy. On the other hand, induced fractures might generate even stronger amplification and site effects.

At frequencies greater than 2 Hz, we could identify additional peaks in our analysis of SRSR. Although the resolved amplification was also directional, polarization orientations were not consistent across the array and amplification maps present a complex spatial pattern. Moreover, no coherently propagating seismic waves were identified with *f–k* analysis at these frequencies. Ground motion above 2 Hz therefore appears to be controlled by vibration of smaller, localized rock mass compartments within the instability.

8 CONCLUSIONS

Measurements presented in this paper support our hypothesis that ambient vibration of a large, potentially unstable rock slope is dominated by normal mode motion. Since the same conclusion was previously postulated at another slope instability in the same area (BU10), we suggest that this phenomenon is not rare. Although the results presented in this study were obtained using seismic arrays, polarization analysis could be performed with single-station noise measurements (point by point). The density of measurement points is critical for correct interpretation of the slope's seismic response. Strong directional amplification was linked to the internal structure of the rock mass, specifically to systematic fracture opening caused by slope movement, rather than topography. Detailed interpretation of the low-frequency response (<1 Hz) would require longer measurement intervals. The resolved fundamental frequency of the instability could be monitored in the future (as in Lévy *et al.* 2010), to asses any potential temporal changes related to internal damage that may precede failure.

ACKNOWLEDGMENTS

The authors would like to thank Antonio Rovelli, and an anonymous reviewer for constructive comments and helpful suggestions. This research is part of the project COGEAR, funded by the Competence Center for Environment and Sustainability of the ETH Domain (CCES). Wavelet software was provided by C. Torrence and G. Compo, available at http://paos.colorado.edu/research/wavelets/. Some figures in this paper were made using Generic Mapping Tools (GMT) 4 by Wessel & Smith (1998).

REFERENCES

Andrews, D.J., 1986. Objective determination of source parameters and similarity of earthquakes of different size, in *Earthquake Source Mechanics,* pp. 259–268, eds Das, S., Boatwright J. & C.H. Scholz, American Geophysical Union, Washington, DC.

Assimaki, D., Gazetas, G. & Kausel, E., 2005. Effects of local soil conditions on the topographic aggravation of seismic motion: parametric investigation and recorded field evidence from the 1999 Athens earthquake, *Bull. seism. Soc. Am.,* **95**(3), 1059–1089.

Asten, M.W. & Henstridge, J.D., 1984. Array estimators and use of microseisms for reconnaissance of sedimentary basins, *Geophysics,* **49,** 1828–1837.

Bard, P.-Y. & Bouchon, M., 1985. The two-dimensional resonance of sediment-filled valleys, *Bull. seism. Soc. Am.,* **75,** 519–541.

Bard, P.-Y., Cadet, H., Endrun, B., Hobiger, M., Renalier, F. *et al*., 2010. From non-invasive site characterization to site amplification: recent advances in the use of ambient vibration measurements, in *Earthquake Engineering in Europe, Geotechnical, Geological, and Earthquake Engineering,* ed. Garevski M., Vol 17, doi:10.1007/978-90-481-9544-2_5, Springer, Dordrecht.

Bearth, P., 1964. Geologischer Atlas der Schweiz – Erläuterungen zum Blatt Randa, Geologischer Atlas der Schweiz 1:25000. Kümmerly & Frey, Bern, 27 pp.

Bensen, G.D., Ritzwoller, M.H. & Yang, Y., 2009. A 3D shear velocity model of the crust and uppermost mantle beneath the United States from ambient seismic noise, *Geophys. J. Int.,* **177,** 1177–1196.

Bonnefoy-Claudet, S., Cornou, C., Bard, P.-Y., Cotton, F., Moczo, P., Kristek, J. & Fäh, D., 2006. H/V ratio: a tool for site effects evaluation. Results from 1D noise simulations, *Geophys. J. Int.,* **167,** 827–837.

Borcherdt, R.D., 1970. Effects of local geology on ground motion near San Francisco Bay, *Bull. seism. Soc. Am.,* **60,** 29–61.

Burjanek, J., Stamm, G., Poggi, V., Moore, J.R. & Fäh, D., 2010. Ambient vibration analysis of an unstable mountain slope, *Geophys. J. Int.,* **180,** 820–828.

Capon, J., 1969. High resolution frequency wavenumber spectrum analysis, *Proc. IEEE,* **57,** 1408–1418.

Curtis, A., Gerstoft, P., Sato, H., Snieder, R. & Wapenaar, K., 2006. Seismic interferometry turning noise into signal, *Leading Edge,* **25,** 1082–1092, doi:10.1190/1.2349814.

Danneels, G., Bourdeau, C., Torgoev, I. & Havenith, H.-B., 2008. Geophysical investigation and dynamic modelling of unstable slopes: case-study of Kainama (Kyrgyzstan), *Geophys. J. Int.,* **175,** 17–34, doi:10.1111/j.1365-246X.2008.03873.x.

Del Gaudio, V. & Wasowski, J., 2007. Directivity of slope dynamic response to seismic shaking, *Geophys. Res. Lett.,* **34,** L12301, doi:10.1029/2007GL029842.

Del Gaudio, V. & Wasowski, J., 2011. Advances and problems in understanding the seismic response of potentially unstable slopes, *Eng. Geol.,* **122**, 73–83, doi:10.1016/j.enggeo.2010.9.007.

Geli, L., Bard, P.-Y. & Jullien, B., 1988. The effect of topography on earthquake ground motion: a review and new results, *Bull. seism. Soc. Am.,* **78**(1), 42–63.

Di Giulio, G., Cara, F., Rovelli, A., Lombardo, G. & Rigano, R., 2009. Evidences for strong directional resonances in intensely deformed zones of the Pernicana fault, Mount Etna, Italy, *J. geophys. Res.,* **114,** B10308, doi:10.1029/2009JB006393.

Fäh, D., Stamm, G. & Havenith, H.-B., 2008. Analysis of three-component ambient vibration array measurements, *Geophys. J. Int.,* **172,** 199–213.

Fäh, D. *et al.*, 2011. ECOS-09 earthquake catalogue of Switzerland release 2011. Report and Database. Public catalogue, 17.4.2011. Swiss Seismological Service ETH Zürich, Report SED/RISK/R/001/20110417.

Farge, M., 1992. Wavelet transforms and their applications to turbulence, *Annu. Rev. Fluid Mech.,* **24,** 395–457.

Forbriger, T., 2006. Low-frequency limit for H/V studies due to tilt, Extended Abstract 32, Sitzung der Arbeitsgruppe Seismologie des FKPE, Haidhof, Germany.

Fritsche, S. & Fäh, D., 2009. The 1946 magnitude 6.1 earthquake in the Valais: site-effects as contributor to the damage, *Swiss J. Geosci.,* **102,** 423–439, doi:10.1007/s00015-009-1340-2.

Fritsche, S., Fäh, D., Gisler, M. & Giardini, D., 2006. Reconstructing the damage field of the 1855 earthquake in Switzerland: historical investigations on a well-documented event, *Geophys. J. Int.,* **166,** 719–731.

Fritsche, S., Gisler, M., Schwarz, G., Fäh, D. & Kästli, P., 2010. *Historical Earthquakes in the Valais*, COGEAR deliverable 1a.2.1, Swiss Seismological Service, SED/COGEAR/R/002/20100110.

Gischig, V., Amann, F., Moore, J.R., Loew, S., Eisenbeiss, H. & Stempfhuber, W., 2011. Composite rock slope kinematics at the current Randa instability, Switzerland, based on remote sensing and numerical modeling, *Eng. Geol.,* **118,** 37–53.

Havenith, H.-B., Jongmans, D., Faccioli, E., Abdrakhmatov, K. & Bard, P.-Y., 2002. Site effect analysis around the seismically induced Ananevo rockslide, Kyrgyzstan, *Bull. seism. Soc. Am.,* **92,** 3190–3209.

Irikura, H. & Kawanaka, T., 1980. Characteristics of microtremors on ground with discontinuous undergone structure, *Bull. Disas. Prev. Res. Inst.,* **30,** 81–96.

Keefer, D.K., 2002. Investigating landslides caused by earthquakes: a historical review, *Surv. Geophys.,* **23,** 473–510.

Kind, F., Fäh, D. & Giardini, D., 2005. Array measurements of S-wave velocities from ambient vibrations, *Geophys. J. Int.,* **160,** 114–126.

Konno, K. & Ohmachi, T., 1998. Ground-motion characteristics estimated from spectral ratio between horizontal and vertical components of microtremor, *Bull. seism. Soc. Am.,* **88,** 228–241.

Lacoss R.T., Kelly, E.J. & Toksöz, M.N., 1969. Estimation of seismic noise structure using arrays, *Geophysics,* **34,** 21–38.

Lévy, C., Baillet, L., Jongmans, D., Mourot, P. & Hantz, D., 2010. Dynamic response of the Chamousset rock column (Western Alps, France), *J. geophys. Res.,* **115,** F04043, doi:10.1029/2009JF001606.

Marano, K.D., Wald, D.J. & Allen, T.I., 2010. Global earthquake casualties due to secondary effects: a quantitative analysis for improving rapid loss analyses, *Nat. Hazards,* **52,** 319–328, doi:10.1007/s11069-009-9372-5.

Michel C., Guéguen, P., El Arem, S., Mazars, J., & Kotronis, P., 2010. Full scale dynamic response of a RC building under weak seismic motions using earthquake recordings, ambient vibrations and modelling, *Earthq. Eng. Struct. Dyn.,* **39,** 419–441.

Moore, J.R., Gischig, V., Burjanek, J., Loew, S. & Fäh, D., 2011. Site effects in unstable rock slopes: dynamic behavior of the Randa instability (Switzerland), *Bull. seism. Soc. Am.,* **101**, doi:10.1785/0120110127.

Nakamura, Y., 1989. A method for dynamic characteristics estimation of subsurface using microtremor on the ground surface, *Quater. Rep. Railway Tech. Res. Inst. Japan,* **30,** 25–33.

Okada, H., 2003. The microtremor survey method, *Geophysical Monograph Series*, no. 12, Society of Exploration Geophysicists, Tulsa, OK.

Panzera, F., Lombardo, G. & Rigano, R., 2011. Evidence of topographic effects through the analysis of ambient noise measurements, *Seism. Res. Lett.,* **82,** 413–419, doi:10.1785/gssrl.82.3.413.

Pischiutta, M., Cultrera, G., Caserta, A. Luzi, L. & Rovelli, A., 2010. Topographic effects on the hill of Nocera Umbra, central Italy, *Geophys. J. Int.,* **182,** 977–987, doi:10.1111/j.1365-246X.2010.04654.x.

Poggi, V. & Fäh, D., 2010. Estimating Rayleigh wave particle motion from three-component array analysis of ambient vibrations. *Geophys. J. Int.,* **180,** 251–267.

Renalier, F., Jongmans, D., Campillo, M. & Bard, P.-Y., 2010. Shear wave velocity imaging of the Avignonet landslide (France) using ambient noise cross correlation, *J. geophys. Res.,* **115,** F03032, doi:10.1029/2009JF001538.

Rigano, R., Cara, F., Lombardo, G. & Rovelli, A., 2008. Evidence for ground motion polarization on fault zones of Mount Etna volcano, *J. geophys. Res.,* **113,** B10306, doi:10.1029/2007JB005574.

Roten, D. & Fäh, D., 2007. A combined inversion of Rayleigh wave dispersion and 2-D resonance frequencies, *Geophys. J. Int.,* **168,** 1261–1275.

Roten, D., Cornou, C., Fäh, D. & Giardini, D., 2006. 2D resonances in Alpine valleys identified from ambient vibration wavefields, *Geophys. J. Int.,* **165,** 889–905.

Steimen S., Fäh, D., Kind, F., Schmid, C. & Giardini, D., 2003. Identifying 2-D resonance in microtremor wave fields, *Bull. seism. Soc. Am.,* **93,** 583–599.

Tokimatsu, K., 1997. Geotechnical site characterization using surface waves. In: *Proc. 1st Intl. Conf. Earthquake Geotechnical Engineering*, ed. Ishihara, K., Vol 3. Balkema, Rotterdam, pp. 1333–1368.

Torrence, C. & Compo, G. P., 1998. A practical guide to wavelet analysis, *Bull. Am. Meteor. Soc.,* **79,** 61–78.

Vidale, J.E., 1986. Complex polarisation analysis of particle motion, *Bull. seism. Soc. Am.,* **76,** 1393–1405.

Wathelet, M., Jongmans, D., Ohrnberger, M. & Bonnefoy-Claudet, S., 2008. Array performances for ambient vibrations on a shallowstructure and consequences over Vs inversion, *J. Seismol.,* **12,** 1–19, doi:10.1007/s10950-007-9067-x.

Wessel, P. & Smith, W.H.F., 1998. New, improved version of the generic mapping tools released, *EOS, Trans. Am. geophys. Un.,* **79,** 579.

Woods J.W. & Lintz, P.L., 1973. Plane waves at small arrays, *Geophysics,* **38,** 1023–1041.

Yugsi Molina, F.X., 2010. Structural control of multi-scale discontinuities on slope instabilities in crystalline rock (Matter valley, Switzerland), *PhD thesis*, ETH Zurich.

Zywicki, D.J., 1999. Advanced signal processing methods applied to engineering analysis of seismic surface waves, *PhD thesis*, Georgia Institute of Technology.